In situ manipulation of the active Au-TiO2 interface with atomic precision during CO oxidation

Yuan, Wentao; Zhu, Beien; Fang, Ke; Li, Xiao Yan; Hansen, Thomas W.; Ou, Yang; Yang, Hangsheng; Wagner, Jakob B.; Gao, Yi; Wang, Yong

Total number of authors:
11

Published in:
Science

Link to article, DOI:
10.1126/science.abe3558

Publication date:
2021

Document Version
Peer reviewed version

In-situ manipulation of the active Au-TiO_2 interface with atomic precision during CO oxidation

Wentao Yuan[1†], Beien Zhu[2, 4†], Ke Fang[1†], Xiao-Yan Li[4, 5], Thomas W. Hansen[3*], Yang Ou[1], Hangsheng Yang[1], Jakob B. Wagner[3*], Yi Gao[2, 4*], Yong Wang[1*] and Ze Zhang[1]

[1] State Key Laboratory of Silicon Materials and Center of Electron Microscopy, School of Materials Science and Engineering, Zhejiang University, Hangzhou, 310027 China

[2] Zhangjiang Laboratory, Shanghai Advanced Research Institute, Chinese Academy of Sciences, Shanghai, 201210 China

[3] DTU Nanolab, Technical University of Denmark, DK-2800, Kgs. Lyngby, Denmark

[4] Key Laboratory of Interfacial Physics and Technology, Shanghai Institute of Applied Physics, Chinese Academy of Sciences, Shanghai, 201800 China

[5] University of Chinese Academy of Sciences, Beijing, 100049 China

[*]Correspondence to: yongwang@zju.edu.cn (Yong Wang); gaoyi@zjlab.org.cn (Yi Gao); thomas.w.hansen@cen.dtu.dk (Thomas Hansen); jakob.wagner@cen.dtu.dk (Jakob Wagner)

[†]These authors contributed equally.

Abstract: The interface between the metal catalyst and the support plays a critical role in heterogeneous catalysis. An epitaxial interface is generally considered "rigid" and tuning its intrinsic microstructure with atomic precision during catalytic reactions is challenging. Using aberration-corrected environmental transmission electron microscopy, we have studied the interface between Au and TiO_2 support. Direct atomic-scale observations show an unexpected dependence of the atomic structure of the Au-TiO_2 interface with the epitaxial rotation of gold nanoparticles on a TiO_2 surface during CO oxidation. Taking advantage of the reversible and controllable rotation, we achieved the in situ manipulation of the active Au-TiO_2 interface by changing gas and temperature. This result suggests that real-time design of the catalytic interface in operating conditions may be possible.

One Sentence Summary: *In situ* manipulating the active Au-TiO_2 interface with atomic precision was realized via epitaxial rotation of Au during CO oxidation.

Supported nanoparticles (NPs) are widely used as catalysts for heterogeneous reactions (*1–7*). Their catalytic activities can depend on the interfaces between the NPs and their substrates because the most active sites in many reactions are located at the perimeter interface (PI) (*7–15*), as is the case for the Au-TiO_2 PI in CO oxidation (*14–16*). Recent in situ experiments indicate that refacetting of NPs and surface reconstructions of the substrates can occur in reactive environments (*17–25*), but little is known about the dependence of the intrinsic interface on the surrounding environment (*26*). Although structural changes of the interface induced by the electron beam (e beam) have been reported (*26–28*), it is unclear whether the intrinsic interface changes in reactive environments, and whether the catalytic interface can be manipulated with atomic precision during reactions (*29–32*).

In this work, by real-time monitoring the Au-TiO_2 interface using environmental transmission electron microscopy (ETEM), we observed that Au NPs strongly anchored on TiO_2 (001) surfaces rotate epitaxially during CO oxidation. Theoretical calculations indicate that this rotation was induced by the change of O_2 adsorption coverage at the PI and demonstrate the change of electronic structure related to the activity of the PI before and after the rotation. Furthermore, through the control of the interfacial O_2 by adjusting the reaction environment, we realized the in situ manipulation of the active Au-TiO_2 interface.

The experiments were performed in a spherical aberration (Cs)-corrected ETEM (FEI Titan 80-300 ST), equipped with a heating holder (DENSsolutions Wildfire S3). To avoid the e-beam induced reconstruction of the interface as reported in previous in situ studies (*26–28*), we chose

to use low e-beam dose (6.45×10^{-1} to 8.73×10^{-1} A/cm^2) and a Gatan OneView CMOS camera in this work to obtain the atomic in situ images of the intrinsic interface structure based on a previous work (*26*). We loaded Au NPs [diameter: 4~8 nm] on TiO_2 nanosheets with dominant (001) surfaces [length: ~30 nm; thickness: ~5 nm] (*33–36*) using impregnation and annealing approaches. The very strong Au-TiO_2 (001) interaction suppressed the sintering of Au NPs (*37*). A low oxygen pressure (~10^{-3} mbar) was first introduced into the ETEM to compensate for the e-beam-induced oxygen loss of TiO_2 nanocrystals. This addition did not change the structures of Au NPs and TiO_2 (001) surfaces, as shown in a recent work (*26*).

A high-resolution TEM (HRTEM) image of the Au-TiO_2 (001) interface structure is shown in Fig. 1A viewed along the TiO_2 [010] direction. The TiO_2 (101) lattice spacings were 0.37 nm, and the Au (111) lattice spacings were 0.24 nm. The interface structure featured atomic steps between TiO_2 (001) and Au (111) crystal planes. The in situ TEM observation showed that this interface structure was stable and did not change after long-term (~20 min) annealing at 500 °C. An image [Fig. 1B] of the atomic structure of the Au-TiO_2 interface of the same NP at 6.5 mbar O_2, three orders of magnitude higher than the low oxygen pressure environment, shows that the (101) lattice fringes are still clearly visible for TiO_2. The Au NP exhibited two sets of lattice fringes with spacings near 0.24 nm that we are assigned to the Au (1-1-1) and (111) planes.

A perfect epitaxial relationship was found at the interface between the Au NP and the TiO_2 (001) surface, i.e., Au NP (111) // TiO_2 (001) (Au NP [01-1] // TiO_2 [010], also see Fig. 1D); we refer to this configuration as $S^{//}$. Compared to Fig. 1A, the interface at high oxygen pressure became atomically smooth and formed a semicoherent interface. The periodic misfit dislocations can be identified at the interface (Fig. 1B) with an extra Au (-111) plane appearing every two

TiO_2 (101) planes. The different interface structures observed at different oxygen pressures indicate that the Au-TiO_2 nanocatalyst changed its interface structure with changing O_2 pressure.

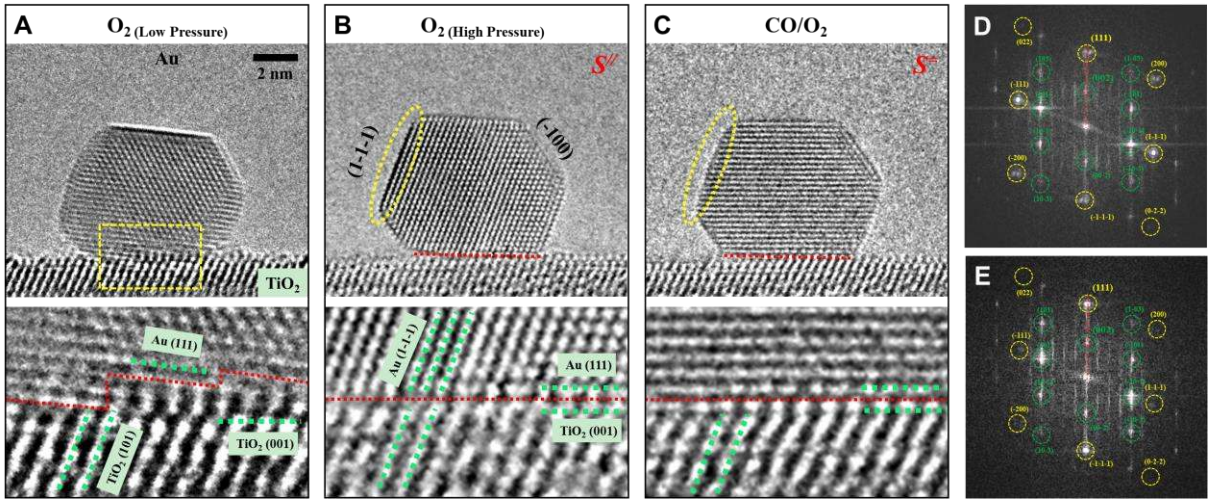

Figure 1. The tunable Au-TiO_2 (001) interface under different gas environments (side view). The temperature is held at 500 °C. The Cs-corrected ETEM images of an Au NP supported on the TiO_2 (001) surface in (**A**) a low-pressure oxygen (10^{-3} mbar), (**B**) a high-pressure oxygen (6.5 mbar) and (**C**) a CO oxidation (total pressure: 4.4 mbar, V_{O2}:V_{CO} = 1:2) environments. The enlarged images of the Au-TiO_2 interfaces [marked by the yellow rectangle in (A)] in different environments are shown below (A), (B) and (C). (**D** and **E**) The fast Fourier transform (FFT) patterns of the Au-TiO_2 catalyst in (B) and (C), respectively. The FFT spots of Au and TiO_2 are labeled by the yellow and green dashed cycles, respectively.

To mimic the reaction condition of CO oxidation, CO was injected into the system, and the O_2 was adjusted to meet the ratio of V_{O2}:V_{CO} =1:2, with a total pressure of 4.4 mbar. The HRTEM image of the Au-TiO_2 interface after exposure to the reaction condition for ~3 min (Fig. 1C) shown that the interface structure changed further in response to the more reducing environment. We kept the e-beam off between Fig. 1, B and C, which excludes the effect of e-beam on the interfacial changes. The disappearing of two-dimensional (2D) lattice fringes of the Au NP shows that the [01-1] zone axis of the Au NP was no longer parallel to the direction of observation (TiO_2 [010]).

Only one-dimensional (1D) Au (111) lattice fringes could be identified—the interface remained atomically smooth with Au (111) attached to TiO_2 (001), this configuration is referred to as $S^{=}$.

Because the lattice fringes of the whole (not a part of) Au NP changed in our observation, we can exclude the possibility that it is induced by surface reconstructions of the Au NP. Note that (1) the TiO_2 crystal lattice showed no notable change compared with Fig 1B, so the TiO_2 substrate remained immobile during the entire process; (2) the Au (111) planes kept parallel to the TiO_2 (001) surface during the rotation (Fig. 1, B to E). Thus, we conclude that from $S^{//}$ to $S^{=}$, a rotation of the Au NP along the axis (Au [111]) perpendicular to the TiO_2 (001) surface (i.e., epitaxial rotation) occurred, which is echoed in the top-view experiments (see below in Fig. 2). For comparison, if the Au NP rolls along another axis, the Au (111) planes will tilt an angle to the TiO_2 (001) surface, as demonstrated in the schematic Fig. S1. All of the results described above support an epitaxial rotation of Au NP on TiO_2 surface induced by environmental change, which suggests the atomic configuration of the Au-TiO_2 interface could be manipulated by controlling external environments.

The top-view observations were obtained to help quantify the rotation angle. Figure 2 shows top-view TEM images of another Au NP located on a TiO_2 nanosheet. To reduce the contrast interfering of the overlapping between Au and TiO_2, the sample was slightly tilted off the zone axis of TiO_2 [001]. The (100) and (010) lattice fringes of TiO_2 still could be identified (yellow line in Fig. 2). The projection of the Au NP was approximately hexagonal with the interior angles of around 120°, indicating the observation direction was very close to the Au [111] zone axis. The FFT pattern in Fig. 2C verified that the epitaxial relationship was consistent with the side view result {Au [111] // TiO_2 [001] and Au (01-1) // TiO_2 (010)} although some spots of Au were not strong due to the slightly tilted sample and the interfering of the TiO_2 substrate. The hexagonal Au

projection could serve as a very good reference for identifying the in-plane rotation. At 500 °C under 5 mbar O_2 pressure, a hexagonal side was parallel to the TiO_2 (010) lattice fringes ($S^{//}$, Fig. 2A). At the same temperature, with the addition of CO, the hexagonal Au NP rotated and the hexagonal side was no longer parallel to the TiO_2 (010) lattice fringes ($S^{=}$, Fig. 2B). The measured rotation angle was ~9.5 °, quantified by comparing Fig. 2B with 2A and confirmed by the FFT pattern in Fig. 2D.

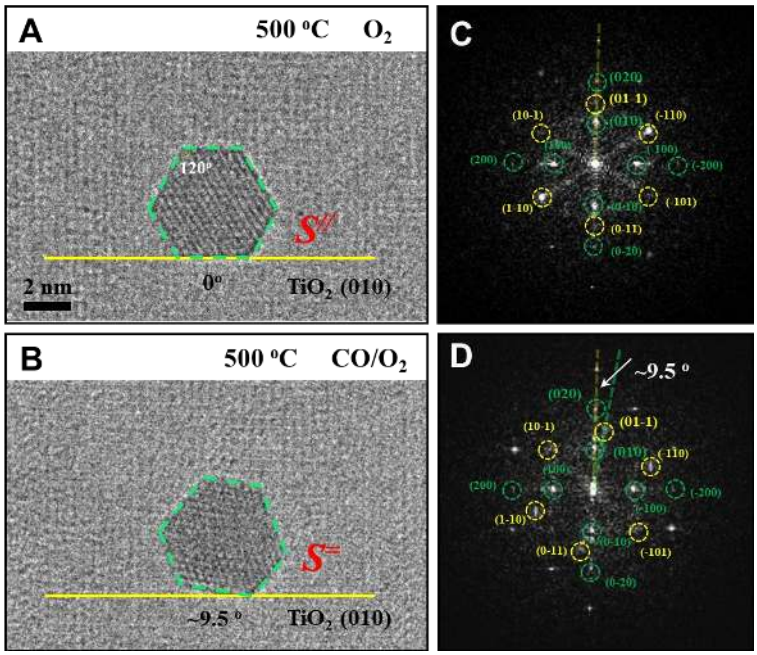

Figure 2. The rotation of a Au NP on the TiO_2 (001) in different environments (top view). (**A–B**) Top view ETEM images show the structural evolution of the Au-TiO_2 (001) nanocatalyst from an oxygen environment [(A), 5 mbar] to a reactive environment [(B), 500 °C, total pressure: 5 mbar, V_{O2}:V_{CO} = 1:2)]. (**C** and **D**) The FFT patterns of the Au-TiO_2 catalyst in (B) and (C), respectively. The FFT spots of Au and TiO_2 are labeled by the yellow and green dashed cycles, respectively.

DFT calculations were performed to obtain insight into the rotation behavior in different environments. A truncated octahedral cluster (Au_{116}) was used as an ideal model for the face-

centered-cubic Au NP. The gold cluster was deposited on a TiO_2 slab, and the contact interface is TiO_2 (001) and Au (111) based on the ETEM observations. The $S^{//}$ was first modelled as a reference (Fig. 3B), according to the featured 2D crystal lattice of the Au cluster viewing along the TiO_2 [010] direction (Fig. 1B). A sequence of test configurations was set up by the clockwise and counterclockwise rotation of the reference Au cluster in small angles (Fig. S2). The energy-calculation results showed that without O_2 adsorption $S^{//}$ became unfavorable in energy, 0.3 eV higher in energy than the most stable configuration. The Au NP of the most stable one (Figs. 3A and 1C) has 1D lattice fringes and was identified as the $S^{=}$ observed in our experiments. The rotation angle between this configuration and the $S^{//}$ was ~8° (Fig. S2), which is near the experimental measurements (~9.5°, Fig. 2, C and D).

The effect of O_2 adsorption was investigated by calculating its adsorption coverage θ at the PI of modeled $S^{//}$ and $S^{=}$, respectively, by combining the DFT calculated adsorption energy (E_{ads}) and the Fowler-Guggenheim adsorption isotherm (details in the Supplementary Materials). Under the experimental condition (500 °C, 5 mbar O_2), O_2 barely adsorbed at the PI of $S^{=}$ ($\theta_{S^{=}}$ is 0.08), whereas the $\theta_{S^{//}}$ was 0.31. The total O_2 adsorption energies at the PI of $S^{//}$ and $S^{=}$ are -4.42 eV and -0.77 eV respectively, which caused $S^{//}$ to be 3.35 eV more stable than $S^{=}$ in such a condition. Similar results were obtained using a truncated-octahedral Au_{79} cluster as well (see the Supplementary Materials). When CO molecules were introduced, they consumed the O_2 at interface (*38*). Direct effects of CO adsorption on the rotation could be excluded because CO does not prefer the perimeter site (*39*), but CO adsorbed on the Au NP could easily react with the O_2 at the PI to form CO_2 (Fig. S6) (*39*, *40*). As the coverage of interfacial O_2 molecules decreased, the stability of $S^{//}$ decreased and the Au NP rotated to $S^{=}$ (refer to Figs. 1 and 2).

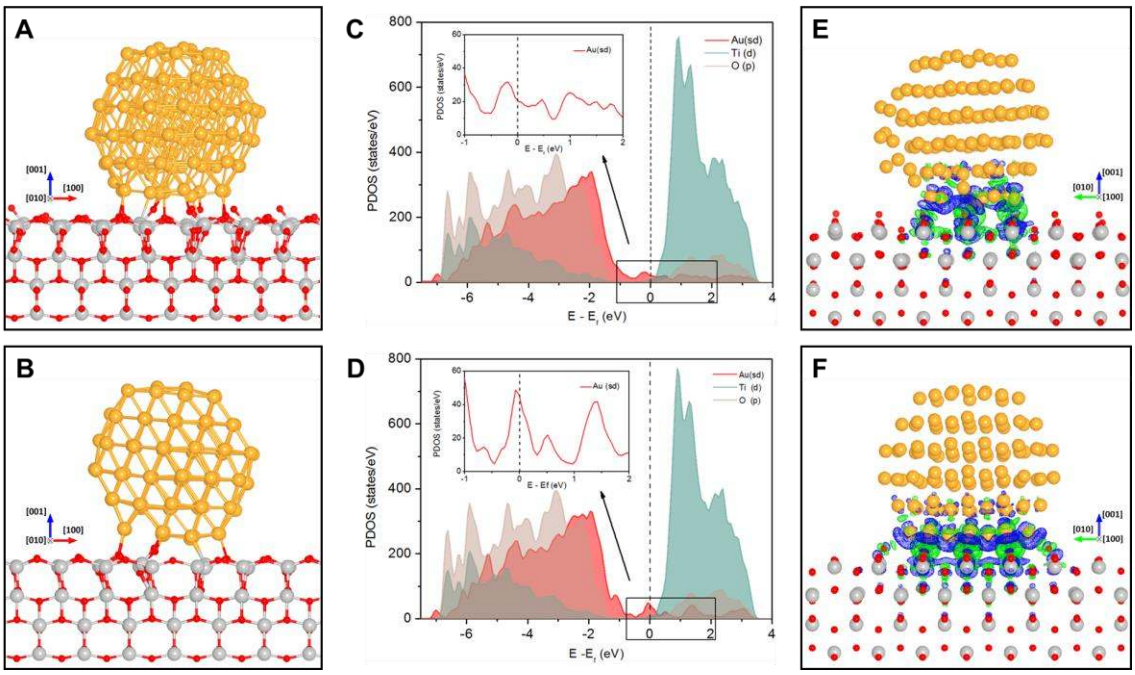

Figure 3. Electronic structure analysis of the supported Au_{116} cluster with $S^{=}$ (A, C, and **E) and $S^{//}$ (B, D,** and **F) configurations.** (**A-B**) The side view of the theoretically identified $S^{//}$ and $S^{=}$ configurations of Au_{116}/TiO_2 (001). (**C-D**) Density of states of the supported Au_{116} cluster. (**E-F**) Three-dimensional charge density difference of the supported Au clusters with isosurface value of 0.002 e/Bohr^3, green for gaining electrons and blue for losing electrons.

The density of states of the two configurations (Fig. 3, C and D) showed that occupied orbitals of Au at the Femi level upshifted toward the Femi level from Au_{116}-$S^{=}$ to Au_{116}-$S^{//}$, so Au_{116}-$S^{//}$ would lose electrons more readily than Au_{116}-$S^{=}$ and would bond more strongly with O_2. Charge-density difference calculations also showed that the interfacial Au atoms of Au_{116}-$S^{//}$ lose more electrons than Au_{116}-$S^{=}$ (enlarged blue region in Fig. 3E-F). The Bader charge calculations also show the number of Au^+ ions with larger positive charges (>0.1 *e*) at the interface are increased from 4 ($S^{=}$) to 9 ($S^{//}$). Previous studies have shown the Au^+ sites can help the adsorption and activation of O_2 at the PI (*40*). It explains why the $S^{//}$ can adsorb more O_2 and also indicates a promoted catalytic activity could be realized by tuning PI with $S^{//}$.

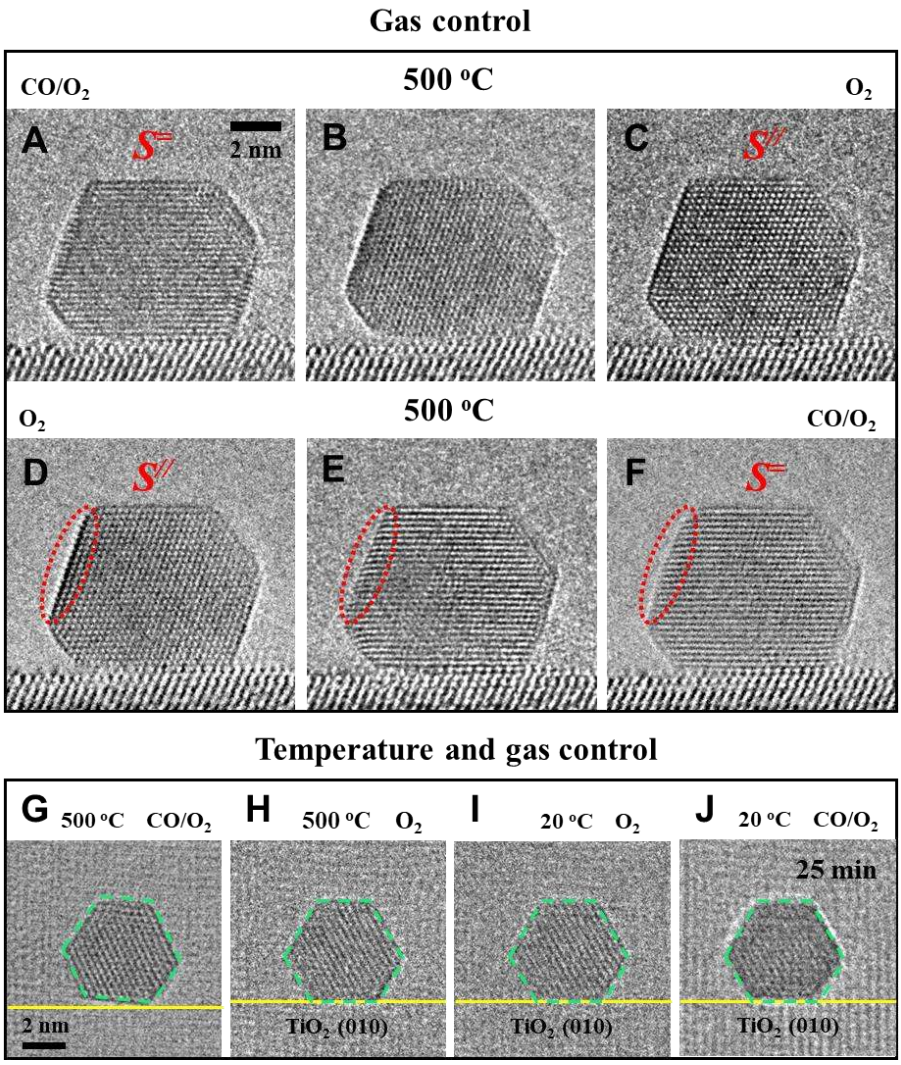

Figure 4. Manipulating Au-TiO_2 (001) interface configurations through an environment dependent rotation. Side-view ETEM images show the structural evolution of the Au-TiO_2 (001) nanocatalyst (**A** and **C**, **B** is the snapshot between A and C) from a reactive environment [(A), total pressure: 4.4 mbar, V_{O2}:V_{CO} = 1:2)] to an oxygen environment [(C) 1 mbar]; (**D** and **F**, **E** is the snapshot between D and F) from an oxygen environment [(D) 4 mbar] to a reactive environment [(F), total pressure: 5 mbar, V_{O2}:V_{CO} = 1:3)]. The temperature is held at 500°C. (**G** to **J**) Top-view ETEM images show the structural evolution of the Au-TiO_2 (001) nanocatalyst under different temperatures. (G, H) were acquired at 500°C [(G), reactive environment, total pressure: 5 mbar, (V_{O2}:V_{CO} = 1:2). (H), oxygen environment, total pressure: 5 mbar.]. (I and J) were acquired at 20°C [(I), oxygen environment, total pressure: 5 mbar. (J), reactive environment, total pressure: 5 mbar, V_{O2}:V_{CO} = 1:2)]. (J) was acquired after exposing under reactive environment for 25 min.

The discovery of NP rotation showed that the structure of an active interface could be controlled during catalytic reactions. As illustrated in Figs. 1 and 2, the tuning could be carried out by changing the reactive gas environments. To further confirm the tunability, we periodically stopped injecting CO during the CO oxidation reaction. Intriguingly, when we stopped injecting CO and reverted to an O_2 environment (1 mbar; Fig. 4A acquired a few minutes after Fig. 1C), a reverse change from $S^{=}$ to $S^{//}$ was observed (Fig. 4, A to C). When the O_2 pressure changed from 1 mbar (Fig. 4C) to 4 mbar, the interface structure showed no notable change (Fig. 4D). In Fig. 4, D to F, we again introduced CO, and rotation from $S^{//}$ to $S^{=}$ was observed again (the intermediate stages during the rotations are presented as Fig. 4, B and E, respectively). A typical rotation process was recorded in Movie S1 and more cases were shown in Figs. S7-S10. These results showed that the Au-TiO_2 (001) interface dynamically responding to the external environment at high temperature was reversible.

In order to exploit the promoted activity of the $S^{//}$ interface, it would be necessary to fix the interfacial configuration in the application. Additional top-view observations showed that the rotation of the Au NP in CO/O_2 reactive environments was temperature dependent. Different from the reversible rotation behavior at 500 °C (Fig. 4, G and H, acquired after Fig. 2B), the rotation of Au NP caused by the gas environment change could be frozen by cooling to 20 °C. When the Au NP was cooled down from 500° to 20 °C (Fig. 4, H to I) in oxygen, the $S^{//}$ state was preserved. At 20 °C, CO injection did not induce the rotation of the Au NP and the $S^{//}$ state kept unchanged during the observation of 25 min (Fig. 4J) in CO/O_2 reactive environments. These results indicate the $S^{//}$ configuration is fixed during low-temperature CO oxidation. After raising the temperature to 500 °C, the dynamic change between $S^{//}$ and $S^{=}$ was observed again. Thus, combining gas control and temperature control, the atomic level interface tunability was realized. These results indicate

various approaches towards the in situ control, which paves the way to the design of distinctive catalysts based on these approaches.

REFERENCES AND NOTES

1. A. Corma, Chemoselective Hydrogenation of Nitro Compounds with Supported Gold Catalysts. *Science*. **313**, 332–334 (2006).

2. G. J. Hutchings, Vapor Phase Hydrochlorination of Acetylene: Correlation of Catalytic Activity of Supported Metal Chloride Catalysts. *J. Catal.* **96**, 292–295 (1985).

3. P. Munnik, P. E. de Jongh, K. P. de Jong, Recent Developments in the Synthesis of Supported Catalysts. *Chem. Rev.* **115**, 6687–6718 (2015).

4. M. Haruta, Gold Catalysts Prepared by Coprecipitation for Low-Temperature Oxidation of Hydrogen and of Carbon Monoxide. *J. Catal.* **115**, 301–309 (1989).

5. A. S. K. Hashmi, G. J. Hutchings, Gold Catalysis. *Angew. Chem. Int. Ed.* **45**, 7896–7936 (2006).

6. D. A. Panayotov, A. I. Frenkel, J. R. Morris, Catalysis and Photocatalysis by Nanoscale Au/TiO_2 : Perspectives for Renewable Energy. *ACS Energy Lett.* **2**, 1223–1231 (2017).

7. M. Valden, Onset of Catalytic Activity of Gold Clusters on Titania with the Appearance of Nonmetallic Properties. *Science*. **281**, 1647–1650 (1998).

8. A. A. Herzing, C. J. Kiely, A. F. Carley, P. Landon, G. J. Hutchings, Identification of Active Gold Nanoclusters on Iron Oxide Supports for CO Oxidation. *Science*. **321**, 1331–1335 (2008).

9. B. Hvolbæk, T. V. W. Janssens, B. S. Clausen, H. Falsig, C. H. Christensen, J. K. Nørskov, Catalytic Activity of Au Nanoparticles. *Nano Today*. **2**, 14–18 (2007).

10. W. Karim, C. Spreafico, A. Kleibert, J. Gobrecht, J. VandeVondele, Y. Ekinci, J. A. van Bokhoven, Catalyst Support Effects on Hydrogen Spillover. *Nature*. **541**, 68–71 (2017).

11. W. Gao, Z. D. Hood, M. Chi, Interfaces in Heterogeneous Catalysts: Advancing Mechanistic Understanding through Atomic-Scale Measurements. *Acc. Chem. Res.* **50**, 787–795 (2017).

12. Y. Suchorski, S. M. Kozlov, I. Bespalov, M. Datler, D. Vogel, Z. Budinska, K. M. Neyman, G. Rupprechter, The Role of Metal/Oxide Interfaces for Long-Range Metal Particle Activation During CO Oxidation. *Nat. Mater.* **17**, 519–522 (2018).

13. D. Widmann, R. J. Behm, Activation of Molecular Oxygen and the Nature of the Active Oxygen Species for CO Oxidation on Oxide Supported Au Catalysts. *Acc. Chem. Res.* **47**, 740–749 (2014).

14. I. X. Green, W. Tang, M. Neurock, J. T. Yates, Spectroscopic Observation of Dual Catalytic Sites during Oxidation of CO on a Au/TiO_2 Catalyst. *Science*. **333**, 736–739 (2011).

15. T. Fujitani, I. Nakamura, Mechanism and Active Sites of the Oxidation of CO over Au/TiO_2. *Angew. Chem. Int. Ed.* **50**, 10144–10147 (2011).

16. M. Haruta, Catalysis of Gold Nanoparticles Deposited on Metal Oxides. *CATTECH*. **6**, 102–115 (2002).

17. E. de Smit, I. Swart, J. F. Creemer, G. H. Hoveling, M. K. Gilles, T. Tyliszczak, P. J. Kooyman, H. W. Zandbergen, C. Morin, B. M. Weckhuysen, F. M. F. de Groot, Nanoscale Chemical Imaging of a Working Catalyst by Scanning Transmission X-Ray Microscopy. *Nature*. **456**, 222–225 (2008).

18. P. L. Hansen, J. B. Wagner, S. Helveg, J. R. Rostrup-Nielsen, B. S. Clausen, H. Topsøe, Atom-Resolved Imaging of Dynamic Shape Changes in Supported Copper Nanocrystals. *Science*. **295**, 2053–2055 (2002).

19. K. F. Kalz, R. Kraehnert, M. Dvoyashkin, R. Dittmeyer, R. Gläser, U. Krewer, K. Reuter, J.-D. Grunwaldt, Future Challenges in Heterogeneous Catalysis: Understanding Catalysts under Dynamic Reaction Conditions. *ChemCatChem*. **9**, 17–29 (2017).

20. T. Uchiyama, H. Yoshida, Y. Kuwauchi, S. Ichikawa, S. Shimada, M. Haruta, S. Takeda, Systematic Morphology Changes of Gold Nanoparticles Supported on CeO_2 during CO Oxidation. *Angew. Chem. Int. Ed.* **50**, 10157–10160 (2011).

21. S. B. Vendelbo, C. F. Elkjær, H. Falsig, I. Puspitasari, P. Dona, L. Mele, B. Morana, B. J. Nelissen, R. van Rijn, J. F. Creemer, P. J. Kooyman, S. Helveg, Visualization of Oscillatory Behaviour of Pt Nanoparticles Catalysing CO Oxidation. *Nat. Mater.* **13**, 884–890 (2014).

22. H. Yoshida, Y. Kuwauchi, J. R. Jinschek, K. Sun, S. Tanaka, M. Kohyama, S. Shimada, M. Haruta, S. Takeda, Visualizing Gas Molecules Interacting with Supported Nanoparticulate Catalysts at Reaction Conditions. *Science*. **335**, 317–319 (2012).

23. W. Yuan, B. Zhu, X.-Y. Li, T. W. Hansen, Y. Ou, K. Fang, H. Yang, Z. Zhang, J. B. Wagner, Y. Gao, Y. Wang, Visualizing H_2O Molecules Reacting at TiO_2 Active Sites with Transmission Electron Microscopy. *Science*. **367**, 428–430 (2020).

24. W. Yuan, Y. Wang, H. Li, H. Wu, Z. Zhang, A. Selloni, C. Sun, Real-Time Observation of Reconstruction Dynamics on TiO_2 (001) Surface under Oxygen via an Environmental Transmission Electron Microscope. *Nano Lett.* **16**, 132–137 (2016).

25. B. Zugic, L. Wang, C. Heine, D. N. Zakharov, B. A. J. Lechner, E. A. Stach, J. Biener, M. Salmeron, R. J. Madix, C. M. Friend, Dynamic Restructuring Drives Catalytic Activity on Nanoporous Gold–Silver Alloy Catalysts. *Nat. Mater.* **16**, 558–564 (2017).

26. Y. Kuwauchi, H. Yoshida, T. Akita, M. Haruta, S. Takeda, Intrinsic Catalytic Structure of Gold Nanoparticles Supported on TiO_2. *Angew. Chem. Int. Ed.* **51**, 7729–7733 (2012).

27. P. Liu, T. Wu, J. Madsen, J. Schiøtz, J. B. Wagner, T. W. Hansen, Transformations of Supported Gold Nanoparticles Observed by *In Situ* Electron Microscopy. *Nanoscale*. **11**, 11885–11891 (2019).

28. Y. Kuwauchi, S. Takeda, H. Yoshida, K. Sun, M. Haruta, H. Kohno, Stepwise Displacement of Catalytically Active Gold Nanoparticles on Cerium Oxide. *Nano Lett.* **13**, 3073–3077 (2013).

29. T. Akita, M. Kohyama, M. Haruta, Electron Microscopy Study of Gold Nanoparticles Deposited on Transition Metal Oxides. *Acc. Chem. Res.* **46**, 1773–1782 (2013).

30. J. J. Liu, Advanced Electron Microscopy of Metal-Support Interactions in Supported Metal Catalysts. *ChemCatChem*. **3**, 934–948 (2011).

31. D. S. Su, B. Zhang, R. Schlögl, Electron Microscopy of Solid Catalysts—Transforming from a Challenge to a Toolbox. *Chem. Rev.* **115**, 2818–2882 (2015).

32. F. Tao, P. A. Crozier, Atomic-Scale Observations of Catalyst Structures under Reaction Conditions and during Catalysis. *Chem. Rev.* **116**, 3487–3539 (2016).

33. H. G. Yang, C. H. Sun, S. Z. Qiao, J. Zou, G. Liu, S. C. Smith, H. M. Cheng, G. Q. Lu, Anatase TiO_2 Single Crystals with a Large Percentage of Reactive Facets. *Nature*. **453**, 638–641 (2008).

34. X. Han, Q. Kuang, M. Jin, Z. Xie, L. Zheng, Synthesis of Titania Nanosheets with a High Percentage of Exposed (001) Facets and Related Photocatalytic Properties. *J. Am. Chem. Soc.* **131**, 3152–3153 (2009).

35. N. Zheng, J. Fan, G. D. Stucky, One-Step One-Phase Synthesis of Monodisperse Noble-Metallic Nanoparticles and Their Colloidal Crystals. *J. Am. Chem. Soc.* **128**, 6550–6551 (2006).

36. G. Li, K. Fang, Y. Ou, W. Yuan, H. Yang, Z. Zhang, Y. Wang, Surface Study of the Reconstructed Anatase TiO_2 (001) Surface. *Prog. Nat. Sci-Mater.* (2020) (doi: 10.1016/j.pnsc.2020.11.002)

37. W. Yuan, D. Zhang, Y. Ou, K. Fang, B. Zhu, H. Yang, T. W. Hansen, J. B. Wagner, Z. Zhang, Y. Gao, Y. Wang, Direct *In Situ* TEM Visualization and Insight into the Facet-Dependent Sintering Behaviors of Gold on TiO_2. *Angew. Chem. Int. Ed.* **57**, 16827–16831 (2018).

38. Y. Chen, P. Crawford, P. Hu, Recent Advances in Understanding CO Oxidation on Gold Nanoparticles using Density Functional Theory. *Catal. Lett.* **119**, 21–28 (2007).

39. Y. Gao, N. Shao, Y. Pei, Z. Chen, X. C. Zeng, Catalytic Activities of Subnanometer Gold Clusters (Au_{16}–Au_{18}, Au_{20}, and Au_{27}–Au_{35}) for CO Oxidation. *ACS Nano*. **5**, 7818–7829 (2011).

40. Z.-P. Liu, X.-Q. Gong, J. Kohanoff, C. Sanchez, P. Hu, Catalytic Role of Metal Oxides in Gold-Based Catalysts: A First Principles Study of CO Oxidation on TiO_2 Supported Au. *Phys. Rev. Lett.* **91**, 266102 (2003).

41. J.F. Creemer, S. Helveg, G.H. Hoveling, S. Ullmann, A.M. Molenbroek, P.M. Sarro, H.W. Zandbergen, Atomic-Scale Electron Microscopy at Ambient Pressure. *Ultramicroscopy* **108**, 993-998 (2008).

42. Y. Jiang, H. Li, Z. Wu, W. Ye, H. Zhang, Y. Wang, C. Sun, Z. Zhang, In Situ Observation of Hydrogen‐Induced Surface Faceting for Palladium–Copper Nanocrystals at Atmospheric Pressure. *Angew. Chem. Int. Ed.* **55,** 12427-12430 (2016).

43. J. Yu, W. Yuan, H. Yang, Q. Xu, Y. Wang, Z. Zhang. Fast Gas–Solid Reaction Kinetics of Nanoparticles Unveiled by Millisecond In Situ Electron Diffraction at Ambient Pressure. *Angew. Chem. Int. Ed.* **57,** 11344-11348 (2018).

44. P. E. Blöchl, Projector Augmented-Wave Method. *Phys. Rev. B* **50**, 17953-17979 (1994).

45. G. Kresse, J. Furthmuller, Efficient Iterative Schemes for Ab Initio Total-Energy Calculations using a Plane-Wave Basis Set. *Phys. Rev. B* **54**, 11169-11186 (1996).

46. G. Kresse, J. Furthmuller, Efficiency of Ab-Initio Total Energy Calculations for Metals and Semiconductors using a Plane-Wave Basis Set. *Comp. Mater. Sci.* **6**, 15-50 (1996).

47. G. Henkelman, B. P. Uberuaga, H. Jónsson, A Climbing Image Nudged Elastic Band Method for Finding Saddle Points and Minimum Energy Paths. *J. Chem. Phys.* **113**, 9901-9904 (2000).

48. http://kinetics.nist.gov/janaf/

ACKNOWLEDGMENTS:

We would like to thank LetPub (www.letpub.com) for providing linguistic assistance during the preparation of this manuscript. **Funding:** We acknowledge the financial support of National Natural Science Foundation of China (52025011, 51390474, 91645103, 11574340, 21773287, 51801182, 11604357, 51872260 and 51971202), the Zhejiang Provincial Natural Science Foundation (LD19B030001) and the Fundamental Research Funds for the Zhejiang Provincial Universities (2019XZZX003-01). B.Z. thanks for the Youth Innovation Promotion Association CAS. The computations were performed on Guangzhou and Shanghai supercomputer centers. W.Y. thanks for China Postdoctoral Science Foundation (2019T120502, 2020M671714). **Author Contributions:** Y. W. initiated the project. Y. W., Y. G. and J. W. supervised the project. W. Y., K. F. and T. H. conducted the ETEM experiments. K. F. and Y. O. prepared the samples, B. Z. and X. L. performed the calculations. H. Y. and Z. Z. participated in the analysis and discussion. W. Y., B. Z. and K. F. contributed equally to this work. **Competing interests:** The authors declare no competing financial interests.

Data and materials availability: All (other) data needed to evaluate the conclusions in the paper are present in the paper, the Supplementary Materials, or the Cambridge Crystallographic Data Centre (Deposition Number: 2044905-2044938).

Supplementary Materials:

Materials and Methods

Supplementary Text

Figs. S1-S11

Table S1

References (41-47)

Movies S1